



# Atmospheric rivers emerge as future freshwater reserves and heat stocks



Mengqian Lu<sup>1,2</sup>✉, Yurong Song<sup>1,2</sup>, Wen Huang<sup>1</sup> & Lujia Zhang<sup>1</sup>

Global atmospheric rivers are major conduits for moisture and energy transport, playing a critical role in the global hydrological cycle and energy redistribution as climate changes. Here, we assess their evolving roles using observations and climate simulations. By 2100, under a high-emission scenario, about 70% of mid-latitude atmospheric rivers are projected to carry more moisture than the Amazon River, with 11% of this intensification driven by future warming. This trend is expected to increase flood risks in densely populated basins such as the Yangtze, Loire, and Sacramento. Moist static energy provides insight into atmospheric rivers' behavior on subseasonal scales. Atmospheric rivers redistribute meridional energy transport during active seasons, a process projected to intensify and shift poleward. Their diverse heat archetypes have varying impacts on precipitation and temperature. These findings highlight the growing influence of atmospheric rivers as dynamic agents of freshwater delivery and heat transport in a warming climate.

The global water cycle is a fundamental process that circulates water among the atmosphere, land, and ocean, balancing energy on Earth's surface through phase changes between vapor, liquid, and solid states. The ocean, as the largest reservoir of saline water, and the land, which provides direct access to freshwater, play pivotal roles in this cycle. Atmospheric rivers (ARs) act as a dynamic highway, linking ocean evaporation to continental precipitation<sup>1</sup>, efficiently transporting water and redistributing energy. A critical function of ARs is the meridional transport of moisture-laden air from the warm tropics to the cooler high latitudes. Along their pathways, ARs release both moisture and latent heat during precipitation, contributing substantial amounts of water to the surface water cycle while warming the lower atmosphere and Earth's surface. This vital water-energy exchange fosters the conditions necessary for life to flourish.

The phenomenon of ARs has sparked considerable debate and extensive discussion. Originally proposed as "Tropospheric Rivers" in the pioneering study<sup>2</sup>, AR was introduced to explain the long-distance transport of carbon monoxide, which could not be adequately accounted for by prevailing wind patterns. Although the term "Atmospheric Rivers" was not coined until 1992, the concept of low-altitude, large-scale moisture streamers had been discussed earlier<sup>3</sup>. Subsequent research has extensively analyzed their climatological<sup>4–7</sup> and hydrological<sup>8–11</sup> impacts, highlighting the crucial role of ARs play in the global water cycle. These narrow, elongated corridors of intense moisture transport in the lower atmosphere were aptly termed "rivers" due to their comparable or even greater magnitude of moisture transport compared to the Amazon River. For instance, Zhu and

Newell<sup>12</sup> estimated AR moisture transport at approximately  $2.2 \times 10^8 \text{ kg s}^{-1}$ , which is about 38% greater than the flux of the Amazon River. Similarly, Ralph et al. (2017) estimated that the total instantaneous water vapor flux in an average AR is 2.6 times the flow of the Amazon River and roughly equivalent to the flow of 27 Mississippi Rivers<sup>13</sup>. More than 90% of the mid-latitude water vapor flux is transported by ARs<sup>14</sup>. Unlike surface rivers, however, the moisture transported by ARs is continuously released and recharged along their lifecycle and routes, reflecting complex atmospheric processes<sup>15</sup>. In addition to the impact on the water cycle by moisture-laden air, the huge amount of warm moist air from low latitudes also transports substantial heat energy<sup>16</sup> to higher latitudes. During the release process of moisture, a great amount of latent heat will be released. Therefore, ARs can potentially contribute to heat-related extremes<sup>16–20</sup>. Accompanied by substantial amounts of latent and sensible heat, ARs play a critical role in atmospheric energy dynamics.

Given that Earth is warming due to increases in greenhouse gases, it is critical to understand how ARs may respond and change in a warming world<sup>21,22</sup>. Recent projections based on Coupled Model Intercomparison Project Phase 6 (CMIP6) indicate that ARs may occur one to two times more frequently, bring associated increases in rainfall and exhibit a poleward shift<sup>23</sup>. As extreme weather events have become more frequent in recent years, improving the prediction of ARs has become crucial. It is imperative to deepen our understanding and investigate the future roles of ARs in the hydrological cycle and Earth's energy redistribution, which is vital for improving future predictions, enhancing model simulation

<sup>1</sup>Otto Poon Center for Climate Resilience and Sustainability, World Sustainable Development Institute, Department of Civil and Environmental Engineering, The Hong Kong University of Science and Technology, Hong Kong, China. <sup>2</sup>These authors contributed equally: Mengqian Lu, Yurong Song.

✉e-mail: [mengqian.lu@ust.hk](mailto:mengqian.lu@ust.hk)

accuracy, and advancing overall predictability. The increased frequency of ARs raises intriguing scientific inquiries into their future impact, particularly given the uncertainties in precipitation efficiency<sup>24,25</sup> and the non-linear changes in atmospheric circulations<sup>26</sup>. This inquiry compels us to ask fundamental questions: How much water do ARs transport globally across different latitudes from past to future periods? How much heat and energy do they carry, shaping their potential impact on various regions? By quantifying the moisture and heat transported by ARs, we will be able to unveil the vital roles of ARs in the future.

In this paper, we aim to steer future discussions on ARs by addressing the aforementioned questions. We conduct a comprehensive analysis to quantify the changes in moisture and heat energy transported by ARs across historical condition and future climate projections, considering the regional differences in AR characteristics. We explore the roles of ARs from an energy perspective on synoptic-to-subseasonal timescales. While ARs pose considerable challenges due to the immense amounts of moisture and heat they transport, they also offer opportunities to harness these as future resources of freshwater and heat. By integrating both hydrological and energy perspectives, our results not only improve understanding of ARs' fundamental roles in the Earth system but also provide valuable insights for effectively utilizing these resources.

## Results

### Amazon-scale ARs: rising global frequency and basin-wide impacts

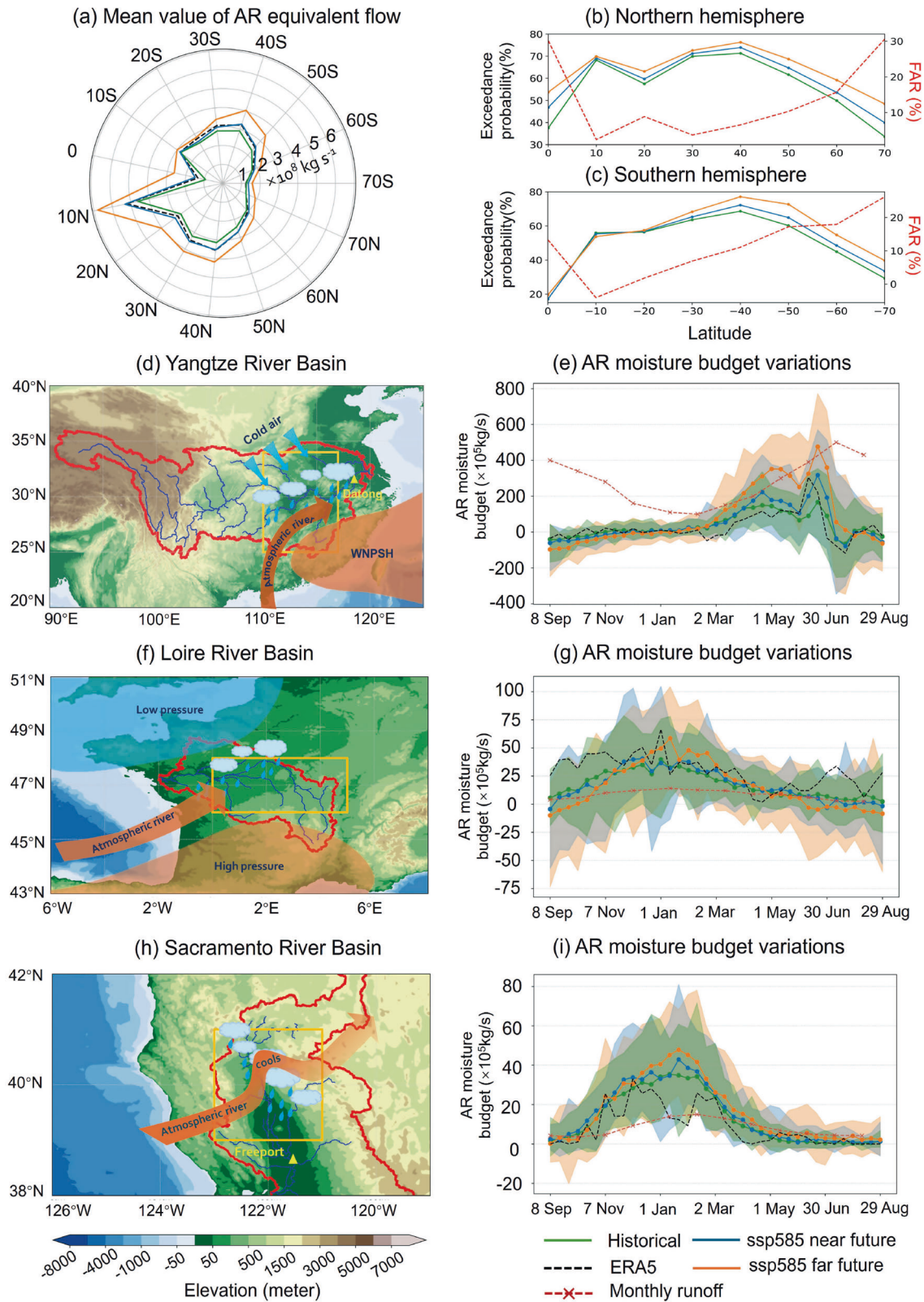
Freshwater constitutes only 0.014% (approximately 200,000 cubic kilometers) of the global water reserves on Earth<sup>27</sup>. The quantity and quality of this scarce resource are essential for the survival of countless lifeforms and human development. Surface rivers provide the most direct access to freshwater resources, with the largest river on Earth, the Amazon River, transporting approximately  $1.6 \times 10^8 \text{ kg s}^{-1}$  of water<sup>13</sup>. To better understand the scale and impact of ARs, the concept of AR equivalent flow is used as a quantitative metric to compare the transport of water vapor in ARs to the flow of water in surface rivers. This metric is defined as the meridional water vapor flux passing through a specific cross-section and is typically expressed as a mass flow rate (unit:  $\text{kg s}^{-1}$ ). It provides an intuitive reference for assessing the magnitude and influence of ARs on the global water cycle. The mid-latitudes (range between 30° and 60° N/S) represent the region with the highest frequency of ARs (Supplementary Fig. S1). These largest rivers in the sky can last from several hours to several days, with an average lifetime of about 40 h<sup>28</sup>. They frequently make landfall along the West Coast of North America, Western Europe, and Eastern China, often resulting in heavy precipitation. Although many studies associate heavy to hazardous precipitation with ARs<sup>10,23,29–32</sup>, they also represent an undeniably important source of freshwater due to the substantial amount of water they transport (Fig. 1a). However, the feasibility of tapping water from ARs remains debatable, both from a technological standpoint<sup>33</sup> and due to potential cross-boundary resource conflicts.

A greater volume of moisture is projected to be transported poleward by ARs. CMIP6-based projections indicate an overall increase in AR meridional moisture flux across latitudes, with the most significant increase (at the 90% significance level based on a *t*-test) occurring in the Northern Hemisphere (Fig. 1a). The scale of Amazon River flow ( $1.6 \times 10^8 \text{ kg s}^{-1}$ ) is used as a benchmark for evaluating the magnitude of moisture transported by ARs. By 2100, the frequency of Amazon River-scale ARs is projected to increase across global latitudes (Fig. 1b, c). Remarkably, approximately 70% of mid-latitude ARs are projected to transport water vapor at levels comparable to or exceeding the scale of the Amazon in the future, surpassing historical levels of 60% (Supplementary Fig. S1). The occurrence of Amazon River-scale ARs is projected to increase more substantially poleward of 40°S and 40°N (Fig. 1b, c). The fraction of attributable risk (FAR; see “Methods”) is used to assess the influence of anthropogenic forcing on the probability of Amazon-scale ARs. Results indicate that FAR increases poleward of 40° in both the Northern and Southern Hemispheres (Fig. 1b, c), with an average of 11% of Amazon-scale ARs in the mid-latitudes attributable to future

warming. This anticipated pattern accentuates the critical need to prioritize research on the impacts of ARs in mid-to-high latitude regions, which are likely to experience profound climatological shifts. Recent studies<sup>23,34</sup> have noted a general poleward shift in AR frequency. Our findings further reveal that intense Amazon-scale ARs will particularly exacerbate hydro-meteorological conditions in mid-to-high latitude regions. These regions, home to flood-prone basins such as the Sacramento, Yangtze, and Loire rivers across various continents, are likely to face amplified impacts from increased and intensified AR activity.

To elucidate the potential hydrological impacts of ARs on river basins, we conducted detailed moisture budget analyses for three distinct river basins affected by ARs: the Yangtze, Loire, and Sacramento (as shown in Fig. 1d, f, h). These basins were selected due to their strong susceptibility to ARs<sup>35,36</sup> and their distinct characteristics, including variations in size, geographic location, and river flow directions. Specifically, the Yangtze flows predominantly west to east, the Loire basin flows north before turning west, and the Sacramento flows primarily southward. The results indicate that the annual peak value of net AR moisture contribution to river basins increases as the climate warms. Specifically, under the SSP585 far-future scenario compared to the historical period, the annual peak increases by 185% for the Yangtze, 47% for the Loire, and 35% for the Sacramento (Fig. 1e, g, i). We observed a strong coherence between the annual cycles of AR moisture contributions and river flows, especially in the flood season, highlighting the crucial role of AR-related precipitation in driving river flow variability. The uncertainty ranges (Supplementary Fig. S2) show that, while all CMIP6 models generally agree, disagreements intensify during flood seasons regarding the magnitude of increases. Specifically, the flood seasons in the Loire and Sacramento River basins align with peak AR moisture contributions from November to April. Meanwhile, the Yangtze River's flood season, from May to September, coincides with the most active period for ARs in East Asia. Although the timing of peak AR activity differs across regions—occurring in summertime in East Asia and in winter in North America and Europe<sup>5,37,38</sup>—these peak periods consistently correspond to the hydrological annual cycles of their respective regions. Under SSP585 scenario, CMIP6 projections indicate a decrease in AR contributions to Yangtze and Loire basins during non-flood seasons, in some months ARs potentially take moisture away from the basins and exacerbate dry conditions, as indicated by the negative values in Fig. 1e, g. Conversely, during the flood seasons, continued warming is expected to increase AR moisture contributions, leading to more intense precipitation events in these basins. This trend suggests a shift toward a more uneven distribution of runoff throughout the year, resulting in a more pronounced amplitude in the annual cycle. These changes are likely to escalate flood risks and challenge water resource management.

In the Yangtze River basin, overall river flow exceeds the AR moisture contribution (Fig. 1e), primarily because AR-related precipitation is concentrated in the lower reaches, while additional water sources, such as snowmelt from the Tibetan Plateau, contribute substantially to the upper Yangtze<sup>39</sup>. The flood season extends from May to October, corresponding to the pre-Meiyu through the summer stages of the East Asia Monsoon<sup>40</sup>. From March to July, ARs provide a positive net moisture contribution, creating an off-peak relationship between the annual cycles of AR moisture contributions and river flows. For the rest of the year, the net moisture contribution from AR is negative, indicating a greater moisture recharge from the lower reaches of the Yangtze to AR than its moisture release. This pattern is projected to intensify under future climate scenarios, with AR net contributions expected to decrease from August to December while increasing substantially from March to July. Such changes could substantially alter the annual cycle of river flows, particularly in the lower Yangtze basin. As a result, proactive management strategies will be essential to address these probable changes, to minimize potential failures to adapt to the evolving environmental conditions and to effectively utilize the resources<sup>33</sup>. The projected increases in moisture flux not only heighten the risk for hydrometeorological extremes<sup>31,32,35,41,42</sup> but also suggest changes in heat fluxes, which will be discussed in the following section.



**Horizontal and vertical heat transport associated with ARs**

ARs play a crucial role in meridional heat transport through the movement of moisture-laden air masses from lower to higher latitudes. These narrow corridors of intense water vapor transport are important carriers of both sensible and latent heat, contributing substantially to the Earth’s energy redistribution<sup>43,44</sup>. The role of ARs in heat redistribution is particularly

crucial in regions where they make landfall and trigger precipitation. The total equivalent water flow (as in Fig. 1) serves not only as an indicator of their hydrological impact but also reflects the amount of latent heat transported. This section examines the pivotal role of ARs in heat transport by analyzing their large-scale horizontal heat fluxes and changes in vertical heat fluxes. Figure 2 depicts the seasonal maps of total sensible heat flux and

**Fig. 1 | Global AR equivalent flows and their impacts on three river basins.** **a** Average AR equivalent flows in the meridional direction at different latitudes (positive values indicate poleward flux;  $\times 10^8 \text{ kg s}^{-1}$ ). **b, c** The solid lines are the exceedance probability of global AR equivalent flow in the meridional direction exceeding Amazon River scale ( $1.6 \times 10^8 \text{ kg s}^{-1}$ ) in the Northern and Southern Hemispheres, the red dashed lines are FAR variations across latitudes. **d, f, h** Schematic maps of the Yangtze River basin, Loire River basin, and Sacramento River basin, showing how they are influenced by ARs. The red lines represent the basin boundaries, while the yellow rectangular boxes indicate the areas used for calculating the AR moisture budget for each basin. Yellow triangles mark the

locations of flow stations in the Yangtze River and Sacramento River basins, whereas the Loire River uses basin-averaged runoff data. WNPSH is the Western North Pacific Subtropical High. **e, g, i** The annual variations of AR moisture budget and river runoff. Red dashed lines represent the monthly average runoff for the three basins, while the other lines show AR moisture budget variations at 10-day intervals under three scenarios: historical (1980–2009, green), SSP585 near future (2025–2054, blue) and SSP585 far future (2070–2099, orange). The shading represents the uncertainty range (the range between the maximum and minimum value) across the CMIP6 models.

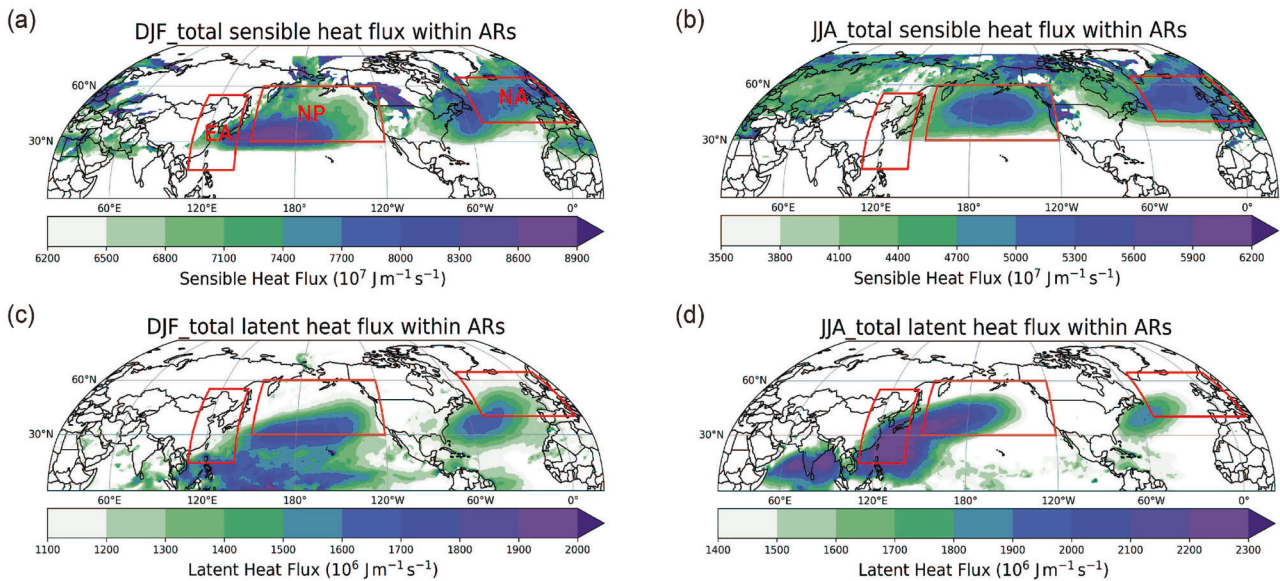


**Fig. 2 | Climatological total sensible heat flux and latent heat flux within ARs derived from ERA5 observations.** **a, b** Total sensible heat flux within ARs for winter (DJF) and summer (JJA), respectively. **c, d** Total latent heat flux within ARs for DJF and JJA, respectively, during the historical period (1980–2014). The colored

rectangle represents three key AR basins affected by the heat flux within ARs: East Asia (EA), North Pacific (NP), and North Atlantic (NA). The value ranges shown for sensible heat flux (**a, b**) and latent heat flux (**c, d**) are different.

latent heat flux carried by ARs in the Northern hemisphere. Next, our analysis will focus on the three key AR basins (hotspots of AR occurrence) in the Northern Hemisphere, as marked in Fig. 2a: (1) Eastern Asia (EA:  $15^{\circ}$ – $55^{\circ}$ N,  $110^{\circ}$ – $140^{\circ}$ E), where ARs interact with complex summer monsoon systems, impacting extreme rainfall events in the Yangtze River basin<sup>23,30,31,45</sup>, (2) North Pacific (NP:  $30^{\circ}$ – $60^{\circ}$ N,  $150^{\circ}$ – $240^{\circ}$ E), where AR development and pathways are influenced by extratropical cyclone dynamics, and (3) North Atlantic (NA:  $40^{\circ}$ – $65^{\circ}$ N,  $50^{\circ}$ W– $15^{\circ}$ E) where ARs are crucial to understanding flooding events in the UK and Western Europe<sup>11</sup>. Additionally, their poleward transports of heat and moisture also potentially affect Arctic sea ice dynamics<sup>46–49</sup>.

ARs carry comparable magnitudes of latent heat flux across the NP and NA basins during boreal winter (DJF). The spatial distribution and intensity of ARs primarily determine the latent heat flux they carry. By aligning the seasonal latent heat flux carried by ARs (Fig. 2c, d) with historical climatological AR frequency maps<sup>23</sup>, a clear consistency emerges. For example, boreal summer (JJA) marks the peak season of AR frequency in EA, where the strong Asian monsoon system dominates latent heat dynamics (Fig. 2d). Despite debates over the characteristics of these intense moisture transports, which are often intertwined with monsoon flows and exhibit wavy shapes unlike those affecting North America and Western Europe, their existence as persistent moisture transport routes in Asia is undeniable. These routes play an indispensable role in the regional global water cycle and energy transport, as evidenced by the quantified fluxes illustrated here.

In contrast, the total sensible heat flux transported by ARs displays more pronounced spatial hotspots and exhibits strong seasonal variability in

magnitude. For instance, during DJF—the peak season of AR activity in the NP and NA basins—the Aleutian Islands and the Bering Strait experience higher AR-carried sensible heat flux compared to JJA (Fig. 2a, b). This wintertime sensible heat flux within ARs correlates strongly ( $r = 0.65$ ) with the intensity of the Aleutian Low-pressure system (Supplementary Fig. S3), suggesting a dynamic interplay between the position and strength of the Aleutian Low and AR activities. Seasonal AR activity near British Columbia and the Gulf of Alaska is closely correlated with the strength of the climatological Aleutian Low<sup>50,51</sup>. The Aleutian Low modulates the path and strength of extratropical cyclones in the North Pacific, which in turn influences the location and intensity of ARs originating from East Asia and impacting the Northern Pacific rim<sup>38,52</sup>. Another notable hotspot of AR sensible heat flux in NA is associated with nor'easters along the upper Atlantic coast of North America, which are closely linked to the AR that frequently causes floods inundating the UK<sup>11,53</sup> and western Europe<sup>32,54</sup>. While sensible heat flux might directly influence regional atmospheric circulation, the release of latent heat is associated with moistening the land surface or contributing to excessive surface runoff (Fig. 1). This dual role underscores the significance of ARs as a bridge between atmospheric circulation and hydrological impacts. The substantial heat flux transported by ARs highlights their important role in redistributing heat within the Earth system. The convergence of horizontal heat flux associated with ARs can lead to considerable surface impacts, such as increased precipitation or the development of heatwaves<sup>19</sup>. The temporal evolutions of total sensible heat flux and latent heat flux within ARs exhibit distinct patterns across the three basins from 1980 to 2009 (Supplementary Fig. S4). As the climate warms,

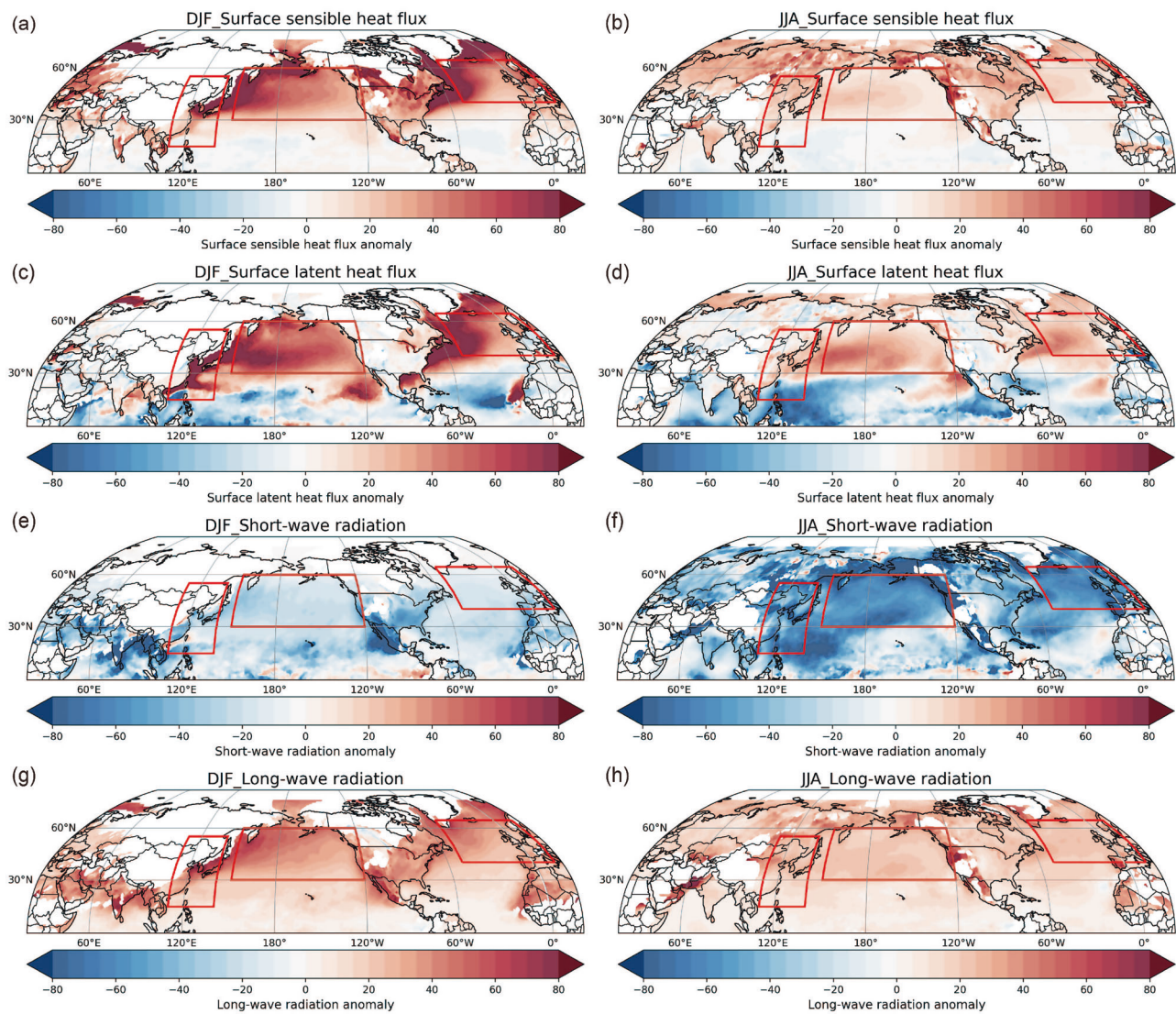


**Fig. 3 | Surface heat flux anomalies within ARs.** Left panels show winter (DJF) and right panels show summer (JJA) AR-associated surface heat flux anomalies during the historical period (1980–2014) for **a, b** sensible heat flux, **c, d** latent heat flux, **e, f** shortwave radiation, and **g, h** longwave radiation (unit:  $W/m^2$ ). Positive values indicate downward anomalies (from the atmosphere to the surface). Anomalies

within ARs are calculated as the seasonal mean heat flux within ARs (Supplementary Fig. S8) minus the climatological mean heat flux (Supplementary Fig. S7) over all AR covered grids. The red rectangle represents three key AR basins affected by the heat flux within ARs: East Asia (EA), North Pacific (NP), and North Atlantic (NA).

the area-averaged sensible heat flux associated with AR remains relatively stable during DJF but shows a decreasing trend during JJA, particularly in the NP and NA basins. In contrast, latent heat flux is projected to increase across all regions and in both seasons under future climate scenarios. These divergent trends indicate a potential shift in the heat transport regimes of ARs. As the climate warms, latent heat flux is anticipated to become the dominant mode of heat transport by ARs, potentially reshaping regional hydrological cycles.

ARs transport substantial sensible and latent heat flux and are associated with seasonal warming anomalies in near-surface air temperature ( $T_{2m}$ ) and sea surface temperature (SST) across all three AR basins. Within identified AR grids, all three basins exhibit  $T_{2m}$  warming anomalies exceeding  $5\text{ }^\circ\text{C}$  in winter (Supplementary Fig. S5a, c, e). In summer, the  $T_{2m}$  anomaly is weaker, around  $1.5\text{ }^\circ\text{C}$  over oceanic areas in NP and NA (Supplementary Fig. S5d), and approximately  $2\text{ }^\circ\text{C}$  over land in the EA basin (Supplementary Fig. S5b). However, Greenland, Canada, the Kamchatka Peninsula, and the Nordic region still exhibit strong  $T_{2m}$  warming anomalies greater than  $5\text{ }^\circ\text{C}$ . Similarly, SST anomalies are stronger and broader in winter—especially around coastal regions—exceeding  $0.5\text{ }^\circ\text{C}$

(Supplementary Fig. S6a, c, e). In contrast, summer SST warming anomalies are not pronounced across the three basins, with most regions instead showing cooling anomalies (Supplementary Fig. S6b, d, f). Warmer summer SST anomalies are mainly observed in the regions where ARs have higher horizontal heat flux (Fig. 2d). These warming anomalies can be linked to changes in vertical surface heat fluxes. For the surface heat flux anomalies associated with ARs (Fig. 3), ARs consistently correspond to a reduction in the climatological upward (negative sign) surface sensible heat flux (Supplementary Fig. S7), reversing the sign of the surface sensible heat flux across NP and NA basins, as well as parts of EA. This results in positive sensible heat flux anomalies (from the atmosphere to the surface) during all seasons when ARs occur. Regarding surface latent heat flux, the upward latent flux is generally reduced during ARs—except in the tropical ocean region of EA (enhanced ocean evaporation in the tropics to supply moisture transport)—resulting in positive anomalies in most areas. Downward shortwave radiation decreases during ARs due to increased cloud cover, while this can be offset by overall positive anomalies in surface longwave radiation, indicating an increase in downward longwave radiation at the surface. For the seasonality, winter exhibits greater surface sensible and latent heat flux

anomalies within ARs (exceeding  $60 \text{ W/m}^2$ ) compared to summer. In ocean basins during summer, the surface latent heat flux within ARs can reverse sign (Supplementary Fig. S8d) relative to the climatological mean (Supplementary Fig. S7d), indicating strong condensation. For shortwave radiation, summer shows a larger negative anomaly (about  $70 \text{ W/m}^2$ ) during ARs due to stronger solar radiation. The increase in downward longwave radiation during winter is greater than in summer, exceeding  $40 \text{ W/m}^2$ . These changes in surface heat fluxes influence the regional total energy balance and, consequently, temperature anomalies within ARs. For example, the positive T2m warming anomaly in winter can be attributed to increased downward sensible heat flux and longwave radiation, as well as reduced upward latent heat flux. These factors can offset the weaker reduction in shortwave radiation, thus maintaining surface warming. During summer, T2m anomalies are weaker and SST warm anomalies are limited to specific parts of the basins, as a greater reduction in shortwave radiation cannot be offset.

### Redistribution of Earth's heat and energy: the role of ARs from an energy perspective

Earth's energy budget exhibits imbalances between higher and lower latitudes, necessitating poleward energy transport via the atmosphere and ocean system. The atmosphere plays a dominant role in this meridional energy redistribution, accounting for 78% of the total heat transport in the extratropics of the Northern Hemisphere<sup>55</sup>. Within this framework, AR emerges as one key contributor. Characterized by their intense water vapor transport from tropics, ARs contribute to the poleward transport of both sensible and latent heat. This transport mechanism is crucial in driving phenomena such as extreme precipitation events<sup>9,56,57</sup> and heatwaves<sup>19,58</sup>. Figure 4 presents the meridional distribution of AR-related energy transport, based on historical data and SSP585 scenario simulations for the near and far future. The distribution of meridional energy transport by ARs in each basin corresponds to their meridional-mean AR frequency, with both curves varying similarly with latitude. Meridional energy, including sensible heat, latent heat transported by ARs, exhibits a consistent increase from historical, through near-future, to far-future periods (Fig. 4a, b), although there is larger uncertainty in the far future. This trend is most pronounced at latitudes where peak heat transport occurs within ARs across all three AR basins. The ongoing intensification over time underscores the strengthening of AR-mediated energy transport in response to enhanced global warming.

The occurrence of ARs enhances poleward sensible and latent heat transport. Seasons with higher AR frequency exhibit stronger magnitudes of heat transport, such as DJF in the NP and NA, and JJA in EA (Fig. 4). The meridional temperature gradient influences the occurrence of ARs and the latitudinal profile of sensible heat transport (SHT). To determine whether the latitudinal distribution of SHT will be influenced by localized or large-scale temperature gradients, we superpose SHT data onto zonal mean T2m differences across various lower latitudes by adjusting the latitude decrement delta,  $\Delta$  (as illustrated in Fig. 4 and detailed in the "Methods" section). We discover that in the NP and NA, the distribution of SHT in ARs aligns more closely with the temperature gradient when  $\Delta$  is set to 5 and 10, respectively, compared to larger  $\Delta$  values, as shown in Fig. 4a and Supplementary Fig. S9. In summer, as temperature differences across the Northern Hemisphere diminish, AR pathways shift northward due to the strengthening of the subtropical high, and AR pathways become primarily driven by larger-scale temperature gradients ( $\Delta = 30$  and  $25$  for the NP and NA, respectively, as indicated in Fig. 4a). In EA, SHT increases steadily with latitude up to approximately  $30^\circ\text{N}$ . Beyond this latitude, AR heat transport begins to diminish, gradually becoming independent of the temperature gradient, until it completely ceases around  $45^\circ\text{--}55^\circ\text{N}$ . This decline in AR heat flux beyond  $30^\circ\text{N}$  can be attributed dynamically to the guidance by the northern flank of the Western North Pacific Subtropical High and the barrier effect of the jet stream.

Meridional latent heat transport (LHT) exhibits comparable strengths in winter and summer across the NP and NA oceanic basins, generally ranging from 1–2 PW (1 PW =  $10^{15}$  W). In contrast, EA shows more

pronounced seasonal variations, with notably higher LHT extending over a notable meridional range from lower altitudes to approximately  $30^\circ\text{N}$  in summer. The meridional distribution of LHT closely follows the latitudinal profile of large-scale meridional moisture gradients ( $\Delta = 30, 40,$  and  $15^\circ$  for NA, NP, and EA, respectively) depicted in Fig. 4b. These findings suggest that AR-associated LHT is primarily influenced by moisture sources from lower latitudes. ARs not only reflect local humidity variations but are more indicative of long-distance moisture redistribution and transport mechanisms, emphasizing again the dual role of AR in the global water cycle and Earth's heat transport and redistribution, the latter is the critical driver for atmospheric processes. Beyond  $30^\circ\text{N}$ , LHT in EA gradually decreases, primarily due to a limited moisture supply and dynamical constraint by the position of the jet stream. In winter, the jet stream shifts southward compared to its summer position, resulting in the peak meridional moisture gradient occurring further south than in summer. This dynamic adjustment underscores the role of AR as a vital marker of complex atmospheric dynamics.

Moist static energy (MSE), which represents the total atmospheric energy, is a useful thermodynamic variable in climate science. Rather than using moisture indicators like integrated water vapor and water vapor transport to describe the structure and dynamics of ARs, we aim to explore ARs from an energy perspective. Poleward transport of MSE helps reduce the energy surplus over the subtropics and tropics, with ARs—acting as long, narrow corridors of moisture to higher latitudes—playing a crucial role in this process. Under global warming, poleward MSE transport is projected to increase at nearly all latitudes<sup>59,60</sup>, and the MSE transported by ARs also increases across all three basins and at all latitudes in the future (Fig. 4c). ARs make a substantial contribution to poleward MSE transport and its increase. During the AR active season in each basin (JJA in EA, DJF in NA and NP), ARs change the climatological latitudinal distribution of total MSE poleward transport (different latitudinal distributions in EA JJA, NP DJF, NA DJF between AR transport and seasonal total transport). In the future, ARs exhibit a global poleward shift<sup>34</sup>, with the peak latitude of meridional MSE transport under the SSP585 far-future scenario also shifting poleward in all three basins. For sensible and latent heat transport, the NP and NA basins also show obvious poleward shifts in the peak of heat energy transport. Therefore, in the context of climate warming, ARs will play an increasingly important role in redistributing energy over the Earth's surface.

ARs play important roles from synoptic to subseasonal timescales. Using daily AR data, successive AR pathways are connected to document a complete lifecycle of each AR event<sup>31</sup>. When ARs traverse the North Pacific, they can travel long distances from East Asia to North America, persist for longer durations on a subseasonal scale, and exert greater impacts<sup>38</sup>. These ARs are fueled by subtropical outflows along the Asian summer monsoon plume, which continuously transport warm, moist tropical air across the North Pacific basin. During their lifecycle, the moisture undergoes repeated processes of release and recharge. Figure 5 illustrates an example of such an AR event playing the aforementioned role on a subseasonal timescale: this event began on June 20 and ended on July 4, lasting a total of 15 days. The animation of this AR event is provided in the Supplementary Movie 1. The moisture release and recharge processes can be reflected by the positive and negative fluctuations in the MSE tendency within the AR until total MSE stabilize in the end. The energy transported by ARs undergoes changes locally along the pathway, altering the atmospheric column energy distribution in different regions and contributing to variations in MSE. ARs transport moisture from East Asia, releasing it as precipitation along their pathways, then recharging and further developing until making landfall in North America. Moreover, hourly variations in MSE, MSE advection, and sensible heat advection are closely synchronized with changes in AR-related rainfall intensity ( $r > 0.6$ ,  $p < 0.001$ ). In contrast, latent heat advection exhibits a lagged correlation with rainfall intensity, with rainfall responding one time step after changes in latent heat advection ( $r = 0.4$ ,  $p < 0.05$ ). This suggests that, although ARs are typically defined based on moisture component, sensible heat and MSE can also be used to describe AR structure and their impacts. Currently, skill in forecasting ARs at the subseasonal-to-

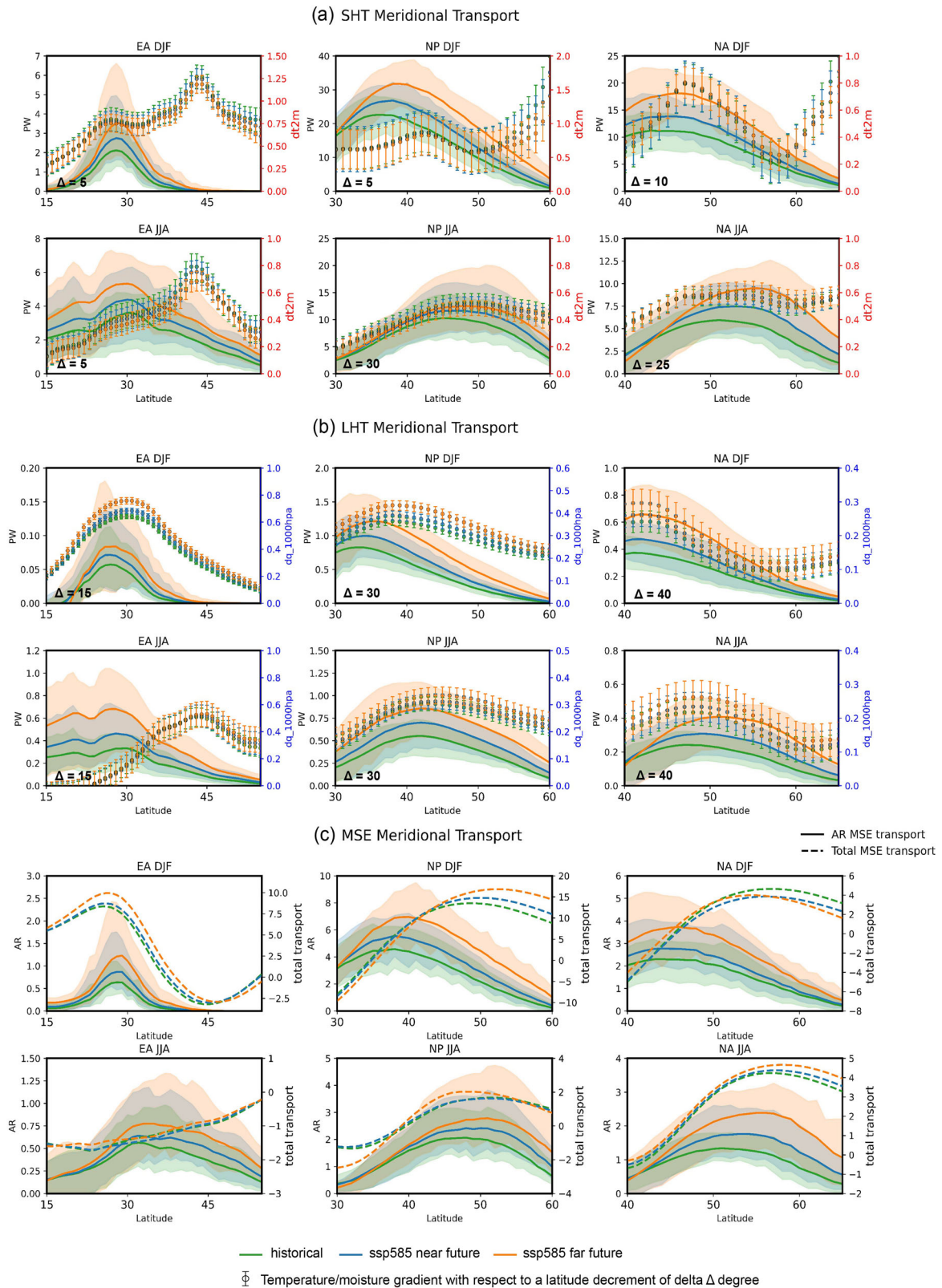
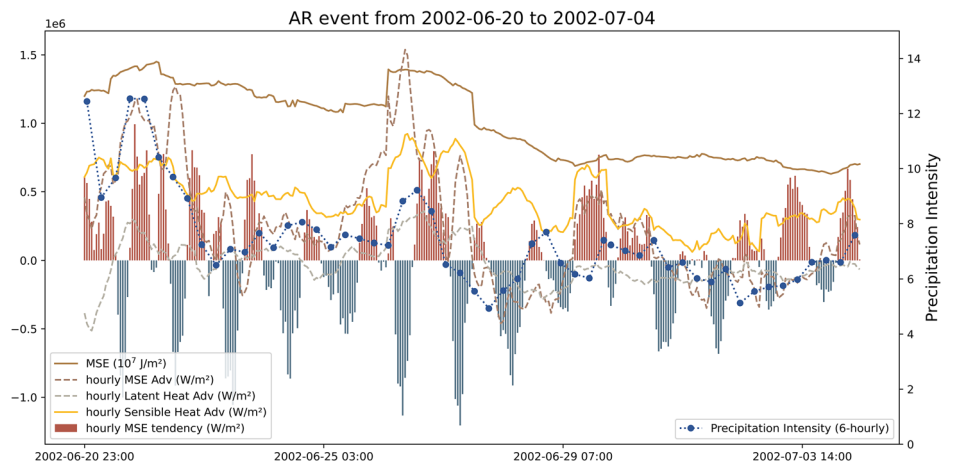


**Fig. 4 | ARs redistribute meridional moist static energy transport during active seasons in three basins. a** Sensible heat energy meridional transport (SHT) by ARs in three basins. **b** Latent heat energy meridional transport (LHT) by ARs in three basins. **c** Moist static energy meridional transport (MSE) by ARs in three basins. The solid lines represent the CMIP6 ensemble mean values, with shading indicating the uncertainty range between the maximum and minimum values, referenced to the left axis ( $1 \text{ PW} = 10^{15} \text{ W}$ ). Scatter points with error bars in (a) and (b) correspond to the

surface temperature gradient (for the SHT map) and the surface specific humidity gradient (for the LHT map), referenced to the right axis (see “Methods”).  $\Delta$  values represent the latitude decrements to calculate meridional gradients. Dashed lines in (c) are the seasonal mean of total MSE meridional transport. The heat transport by ARs is calculated for three scenarios: historical (1980–2009), SSP585 near future (2025–2054), and SSP585 far future (2070–2099). The value ranges differ across seasons and regions.

**Fig. 5 | Evolution of an AR event on subseasonal timescale from energy perspective.** The figure shows the hourly variations of MSE, MSE advection, latent heat advection, sensible heat advection, MSE tendency (bars) within AR, and 6-h precipitation intensity (blue dashed line with circles) during the AR event from June 20 to July 4, 2002.



seasonal timescale remains limited<sup>61</sup>. Analyzing the evolution of ARs from an energy perspective at the subseasonal scale is conducive to developing a deeper mechanistic understanding and may ultimately improve predictions of ARs and their associated heat transport.

### AR heat archetypes and their weather impacts

ARs manifest in various types, each characterized by distinct dynamic or thermal mechanisms that govern their behavior and impacts<sup>62,63</sup>. They transport huge amounts of heat, which is critical in determining their influence on surface weather conditions. Although earlier research has often highlighted the role of ARs in extreme precipitation events, their capacity for transporting heat also critically affects surface temperatures. Recent studies have begun to investigate how ARs can lead to warm winters and extreme heat events by altering surface sensible heat flux<sup>16</sup>, and impacting SST by ageostrophic advection and vertical mixing<sup>18</sup>. Relatively moist and warm ARs carry a large amount of sensible heat flux, expected to increase the downward heat flux and warm the surface. Our study employs total sensible and latent heat fluxes within ARs as orthogonal axes to delineate distinct AR archetypes. We explore how these classifications relate to variations in precipitation and temperature patterns during the peak AR seasons across three key basins: summer in East Asia, and winter in the oceanic basins of the North Pacific and North Atlantic as depicted in Fig. 6. Due to differences in climatology (larger temperature gradients in DJF than JJA), the distribution of total sensible heat flux-latent heat flux within ARs is different in each basin. For EA, there is a weak positive correlation between sensible heat flux and latent heat flux; the two are relatively isolated and exhibit a wide range of values. In the NP, total sensible heat flux and latent heat flux show a positive correlation, with a noticeably skewed distribution. The correlation is strongest in NA, where the distribution is more concentrated and even more skewed. These distinct kernel density distributions indicate that ARs in different regions display different heat archetypes, resulting in varied impacts.

In NA and NP, the relationship between heat archetype and rainfall intensity is less pronounced (Fig. 6b, c). Generally, the top grids of each column (representing higher latent heat flux) exhibit stronger rainfall intensity. Additionally, rainfall intensity increases toward the right grids as sensible heat flux increases. Regarding SST anomalies, ARs characterized by both higher sensible heat flux and latent heat flux (along the positive diagonal) tend to produce greater positive SST anomalies, with the strongest anomalies occurring in the upper right corner of the heatmap (Fig. 6e, f). Strong ocean-atmosphere coupling can be observed in NP and NA, where ARs are associated with about half degree warmer SST than the climatology in coastal regions, such as the Bering Sea, the North American West Coast, Greenland, the European North Sea, and British coastal waters (Supplementary Fig. S10h, l). The climatology of surface sensible heat flux over these

oceans is negative in winter, indicating heat transfer from the ocean to the atmosphere (Supplementary Fig. S10e, i). However, during AR events, the surface sensible heat flux shifts to positive values across most oceanic regions, particularly in coastal areas where warm SST anomalies occur (Supplementary Fig. S10f, j). This shift promotes heat transfer from the atmosphere to the ocean. Stronger ARs enhance this atmosphere-to-ocean heat transfer, thereby contributing to the formation of positive SST anomalies. Notably, the specific physical processes of SST responses to ARs are highly complex, with ocean dynamics partially offsetting atmospheric forcing in some cases<sup>18</sup>. ARs with high sensible heat and latent heat flux are not strictly or linearly positively correlated with SST warming anomalies, emphasizing the importance of detailed investigation on a smaller regional or localized scale.

In summer over East Asia, the impacts of sensible and latent heat fluxes from ARs on surface conditions are more independent. Stronger latent heat flux is linked to heavier rainfall (Fig. 6a), while lower latent heat flux corresponds to warmer land T2m anomalies (Fig. 6d). This suggests that in summer, latent heat flux in ARs plays a dominant role in shaping surface conditions. ARs are associated with an increase in T2m of approximately 1–3 °C in East Asia (Supplementary Fig. S10d), with the most pronounced warming observed in Northern East Asia and the lower Yangtze River Basin. This warming associated with ARs in summer suggests a potential link between lowered latent heat flux within ARs and the occurrence of humid heat wave events in the region. Further analysis reveals the surface heat flux conditions under different levels of latent heat flux ( $Q^L$ ) carried by ARs—days with  $Q^L > 15 \times 10^8 \text{ Jm}^{-1}\text{s}^{-1}$  (Supplementary Fig. S11a) and days with  $Q^L < 15 \times 10^8 \text{ Jm}^{-1}\text{s}^{-1}$  (Supplementary Fig. S11b). Lower latent heat flux within ARs is associated with a reduction in lower cloud cover and a subsequent large increase in total incoming shortwave radiation, which can offset the cooling effect caused by increased evaporation and slightly decreased downward longwave radiation. Therefore, positive land surface temperature anomalies in the lower Yangtze River Basin and the coastal areas of Northern East Asia are strongly associated with AR events characterized by low latent heat flux. Engineering experiments or strategies for tapping AR freshwater should not overlook the possible collateral latent heat release.

The detailed analysis of latent and sensible heat fluxes across various AR regions offers crucial insights into their climatic impacts. Understanding how ARs transport sensible and latent heat is vital for predicting their regional and seasonal influences on surface meteorological conditions, including changes in precipitation, temperature variations, and potential extreme weather events. An emerging consensus suggests that global warming may lead to more frequent and intense AR activity<sup>8</sup>, with varying consequences due to a mix of overall increased latent heat flux and decreased sensible heat in places such as East Asian summers (Supplementary Fig. S4).

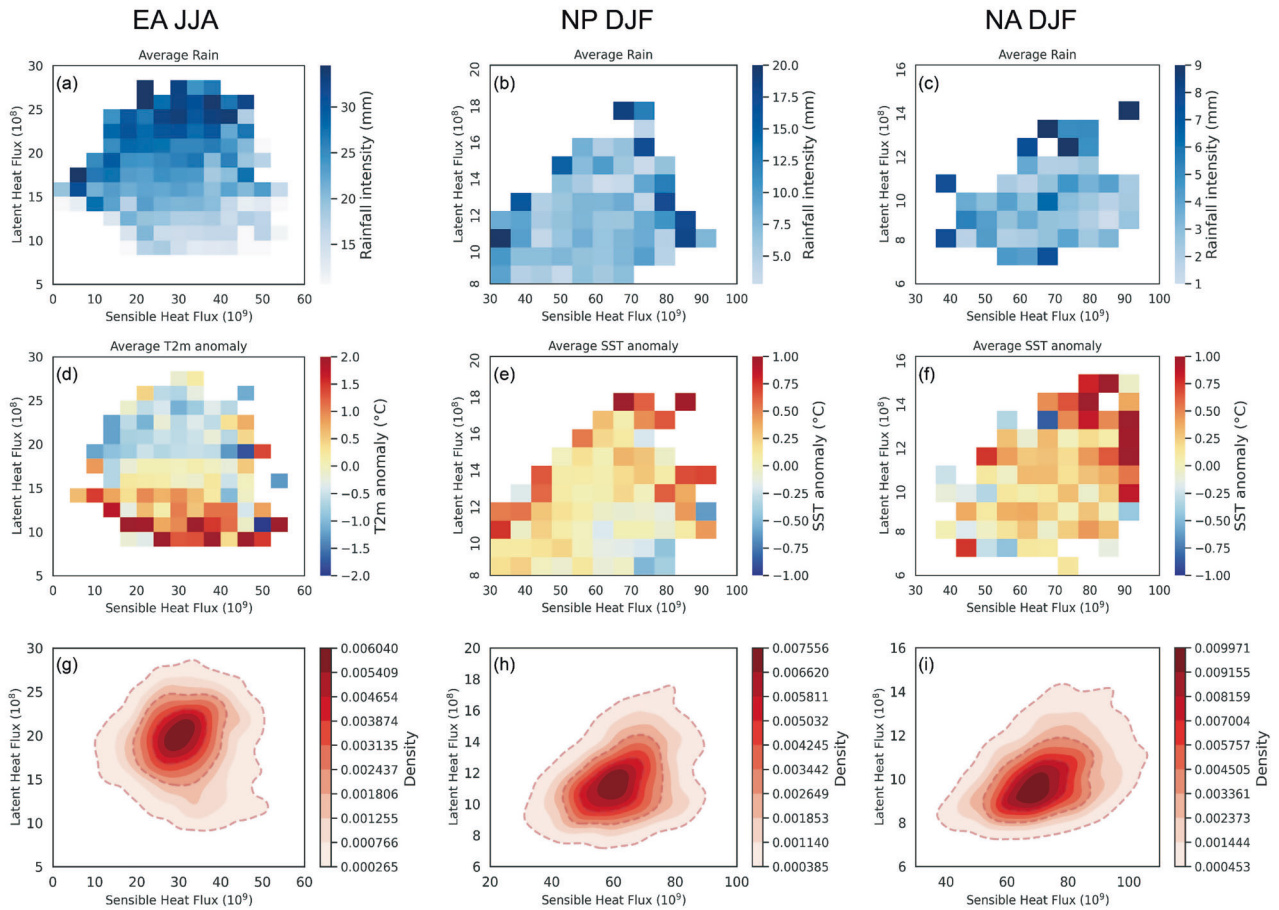


**Fig. 6 | Distinct AR heat archetypes exhibit varying impacts on precipitation and temperature patterns.** **a–c** Heatmaps of average rainfall intensity in AR-related land patches for each AR basin: EA JJA, NP DJF, NA DJF. **d** Heatmap of T2m anomaly of land grids through which ARs pass in EA JJA. **e, f** Heatmaps of winter SST anomaly in the North Pacific (NP) coastal region (30–60°N, 225–240°E) and the North Atlantic (NA) coastal region (40–65°N, 0–15°E), corresponding to regions with

higher SST anomalies shown in Supplementary Fig. S5. These heatmaps show the relationship between different magnitudes of total latent and sensible heat flux within ARs and their associated surface impact. **g–i** Two-dimensional Kernel Density Estimation (KDE) maps for latent heat flux and sensible heat flux, showing the joint distribution of latent heat flux and sensible heat flux for each AR basin.

## Discussion

ARs are key manifestations of climate change impacts on the hydrological cycle and the Earth’s energy redistribution. In this study, we use the scale of Amazon River flow as a benchmark to quantify the magnitude of moisture transported by ARs, and find that, under global warming, the probability of Amazon-scale ARs is projected to increase, particularly at latitudes above 40°S and 40°N. About 70% of mid-latitude ARs are projected to transport moisture exceeding the Amazon River’s flow under SSP585 far-future, with 11% attributable to future warming. In three mid-latitude river basins—the Yangtze, Loire, and Sacramento—a strong coherence is observed between the annual cycles of moisture contributions by ARs and river flows, especially during the flood season, highlighting the crucial role of AR-related precipitation in driving river flow variability. As ARs become more frequent, more intense, and shift geographically, the annual flow patterns and associated hydrological extremes in these densely populated basins are expected to undergo substantial changes. Additionally, ARs can induce seasonal warm anomalies in near-surface air and sea surface temperatures across these key AR basins. These anomalies are associated with large-scale horizontal sensible and latent heat fluxes, as well as related anomalous surface heat exchanges. The heat archetypes of ARs, defined by their heat flux profiles, effectively characterize the regional variations in AR-associated precipitation and temperature patterns. Looking ahead, the poleward transport of heat and total atmospheric energy by ARs is projected to increase, with the peak shifting toward higher latitudes. During active AR seasons, ARs will play a key role in redistributing energy poleward across

latitudes. From an energy perspective, repeated processes of moisture release and recharge on subseasonal timescales can be observed during AR events, underscoring the importance of describing ARs using energy-related variables.

Future changes in AR moisture and heat transports will affect not only regional hydrology but also weather systems, as ARs play a crucial role in heat redistribution, particularly from synoptic to subseasonal timescales, given their typical lifespans of 7–14 days<sup>30,38</sup>, especially in the areas that are under AR main routes. Sensible heat flux is a more direct process linked to surface temperature<sup>16</sup>; the impacts of the changes in AR latent heat flux are complex, as they are influenced by the variability of precipitation efficiency (PE). PE can vary across different regions and times due to a range of atmospheric and topographic conditions<sup>64</sup>. As a result, effective latent heat release depends on both the latent heat flux potential and the prevailing PE. This variability is a key reason why tracking ARs alone does not necessarily improve precipitation predictability<sup>30</sup>. Favorable conditions for precipitation, such as topographic lifting and interactions with extratropical cyclones and frontal systems, must also be present for extreme precipitation to occur<sup>13</sup>. Therefore, only with a robust AR tracking system and reliable forecasts of environmental conditions can we improve the prediction of AR-associated precipitation. This has been demonstrated using a suite of deep learning techniques<sup>65</sup> to enhance AR tagging and prediction. Particular attention should be given to the increased PE during AR events<sup>66</sup>. On average, grid cells affected by ARs exhibit a mean PE of approximately 60% in winter and 50% in summer, calculated as the ratio of daily precipitation to

atmospheric precipitable water (Supplementary Fig. S12). Along the West Coast of North America, winter ARs generally show relatively high PE. In regions where future ARs exhibit enhanced latent heat flux, an associated increase in PE could enable synoptic circulations to draw more moisture from these systems. Such areas may offer opportunities for engineers to explore water tapping schemes, leveraging the increased moisture availability from ARs<sup>23,33</sup>.

ARs transport comparable amounts of moisture into river basins (Fig. 1). However, only a portion of this moisture contributes directly to surface water flow through precipitation, leaving the majority untapped. With the projected increase in the frequency and intensity of ARs in many regions around the world, the potential to harness them as future freshwater and heat stocks is becoming a topic of growing interest. Although this idea still raises debates<sup>67</sup>, both technically and geopolitically, it is crucial to seriously explore this possibility as a viable resource for addressing water scarcity.

From a water resource perspective, ARs represent moving reservoirs of water, often carrying water vapor amounts comparable to the world's largest rivers, with an equivalent flow that exceeds that of the Amazon River. Capturing even a fraction of these "sky rivers" could contribute greatly to securing freshwater reserves, particularly in regions subject to increasing water stress. However, the exploitation of ARs presents considerable scientific, technological and geopolitical challenges. From an engineering standpoint, innovative technologies must be developed to extract water from ARs without disrupting their essential function in the global water cycle and energy balance. In considering ARs as not only vectors of moisture but also as substantial stocks of heat energy, it is crucial to recognize the role of latent heat release during their interaction with local weather systems. As ARs are tapped, the release of latent heat can substantially alter local atmospheric conditions, influencing temperature and pressure dynamics. This process can lead to enhanced cloud formation, increased precipitation, and potentially more intense weather events. Scientifically, there is a need to better understand how ARs interact with atmospheric and hydrological systems to ensure that water extraction does not exacerbate extreme weather events or alter regional climates. On the geopolitical front, the trans-boundary nature of many ARs implies resolving issues of water resource sharing and governance. A cooperative and equitable approach will be crucial to harnessing this water potential and preserving global ecological balance. To address these challenges, it is crucial to conduct in-depth research to map the opportunities and constraints related to the exploitation of ARs in different regions of the globe. This mapping will need to integrate climate projections, hydrological models, technical considerations, and geopolitical issues. This comprehensive approach will aid in defining viable and sustainable adaptation strategies, ensuring that ARs can be leveraged responsibly as future freshwater resources.

While ARs hold promise as a potential freshwater resource, they also pose notable hazards. Addressing these risks through robust mitigation and adaptation strategies is critical. The intense moisture transport and rapid precipitation associated with ARs can lead to catastrophic flooding events, particularly in coastal and mountainous regions. As the climate warms and the moisture-holding capacity of the atmosphere increases, the frequency and intensity of AR-driven floods are projected to escalate in many parts of the world. These events threaten communities, infrastructure, and ecosystems, underscoring the urgency of enhancing flood preparedness and resilience.

Conversely, the atmospheric conditions that fuel ARs can also contribute to prolonged droughts in their wake<sup>68,69</sup>. The diversion of moisture-laden air masses away from certain regions as moisture sources can result in prolonged dry spells and water scarcity, impacting agriculture, water supplies, and natural habitats. This heightens the need for effective water management strategies to mitigate the effects of AR-induced dry periods. Developing effective mitigation and adaptation measures will require a multifaceted approach, drawing on advancements in weather forecasting, early warning systems, infrastructure design, land use planning, and water conservation practices. Collaboration across disciplines, sectors, and borders will be essential to address the complex challenges posed by the dual-

edged nature of ARs—harnessing their benefits while minimizing their hazards.

Ultimately, the successful navigation of AR-related risks and opportunities will be a critical component of building resilient and sustainable communities in the face of a rapidly changing climate. Investing in research, innovation, and coordinated action will be key to unlocking the full potential of these atmospheric phenomena while safeguarding the well-being of people and the environment. By balancing opportunity with caution, ARs can serve as both a vital resource and a manageable risk in the context of global water security and climate resilience.

## Methods

We utilize hourly ERA5 (fifth generation of the European Center for Medium-Range Weather Forecasts) variables<sup>70</sup> from 1980 to 2014 including zonal wind ( $u$ ), meridional wind ( $v$ ), atmospheric temperature ( $T$ ), surface temperature ( $T2m$ ), precipitation ( $pr$ ), sea surface temperature ( $SST$ ), integrated water vapor ( $IWV$ ), integrated water vapor transport ( $IVT$ ) specific humidity ( $q$ ), surface sensible heat flux ( $sshf$ ), surface latent heat flux ( $slhf$ ), surface net solar radiation ( $ssr$ ) and surface net thermal radiation ( $str$ ). All of these variables have been aggregated into daily values for analysis. The monthly variations of river discharge of the Sacramento River at Freeport station, the Yangtze River at Datong station and basin average data in Loire are used. We selected 23 CMIP6 models<sup>71</sup> to investigate the projected changes under the Shared Socioeconomic Pathway 2–4.5 (SSP245) and 5–8.5 (SSP585) (see Supplementary Table S1). The CMIP6 model datasets span from 1980 to 2099, with 2014 serving as the transition point between historical simulations and future projections. To enable comparisons, we focus on three 30-year periods: the historical period (1980–2009), the near-future period (2025–2054), and the far-future period (2070–2099). Our analysis emphasizes ARs during December–January–February (DJF) and June–July–August (JJA), which are the peak seasons for AR frequency. The historical and future daily atmospheric river database<sup>23</sup> applying PanLu 2.0 algorithm<sup>31</sup> is used.

## Calculation of AR equivalent flow and AR moisture budget

Calculate the poleward equivalent flow of each AR at different latitudes each day in Fig. 1a, b, and Fig. S1:

$$Q_{lat} = \sum_{\lambda_1}^{\lambda_2} Q_v(x, \varphi) \times a \tag{1}$$

In the above equation,  $a$  represents the distance of one degree of longitude at different latitudes,  $a = 111 * 10^3 * \cos(\text{pi} * \text{latitude} / 180)$ , the unit is meters. Consider poleward transport as positive.  $\varphi$  represents latitude ranging from 70S to 70N.

The yellow rectangular box in Fig. 1b represents the spatial range for calculating the AR moisture budget for each basin. The AR moisture net budget of the basin is defined as the sum of IVT at the southern, northern, western, and eastern boundaries.

$$Q_T = \sum_{\lambda_1}^{\lambda_2} Q_v(x, H_1) \times a + \sum_{\lambda_1}^{\lambda_2} Q_v(x, H_2) \times a + \sum_{\varphi_1}^{\varphi_2} Q_u(y, V_1) \times b + \sum_{\varphi_1}^{\varphi_2} Q_u(y, V_2) \times b \tag{2}$$

$Q_T$  is net AR moisture flux for each basin,  $b$  represents the distance of one degree of latitude at different longitude, which equals to  $111 * 10^3$  meters;  $Q_u$  &  $Q_v$  are zonal and meridional IVT, respectively ( $\text{kg} \cdot \text{m}^{-1} \cdot \text{s}^{-1}$ );  $x$  and  $y$  is the longitude and latitude of the AR grid point.  $H_1 H_2 V_1 V_2$  are the latitude and longitude corresponding to four boundaries, respectively;  $\lambda_1, \lambda_2 (\varphi_1, \varphi_2)$  represent the longitudes (latitudes) of the west and east (north and south) boundaries grid point of the AR.

### Attribution analysis

The proportion of ARs exceeding the Amazon River scale that is attributable to future warming is assessed using the Fraction of Attributable Risk (FAR)<sup>72</sup>. The equation is given by:

$$FAR = 1 - \frac{P_{hist}}{P_{future}} \quad (3)$$

where  $P_{hist}$  is the exceedance probability in the historical period, and  $P_{future}$  is the exceedance probability under SSP585 far-future scenario.

### AR-related rain patch

The AR-related rain patch is defined as the precipitation that coincides with the AR pathway<sup>38</sup>. However, a significant portion of AR-related precipitation occurs outside the AR pathway. To address this, we also consider precipitation near the boundaries of the AR in this study. First, the daily rain patches are identified by connecting the  $1^\circ \times 1^\circ$  grids where the daily total precipitation exceeds 6 mm. A rain patch must include at least two grids to qualify. Then, rain patches are classified as AR-related if they overlap with the daily AR pathway. We then labeled the grids of AR-related rain patches, along with their corresponding precipitation values. The intensity of daily AR-related rain patch is used in Fig. 6, while the labeled grids are utilized to compute the precipitation efficiency of AR-related rain patches (Supplementary Fig. S12). For Fig. 5, the 6-h precipitation intensity associated with hourly cross-Pacific AR events is calculated as follows: 6-h rain patches are first identified by connecting adjacent  $1^\circ \times 1^\circ$  grids where the total 6-h precipitation exceeds 6 mm; one rain patch should include at least 2 grids. A rain patch is then classified as AR-related if it overlaps with the AR pathway for at least 2 h.

### Calculation of heat flux and energy meridional transport

$$Q^S = g^{-1} c_p \int_{p_t}^{p_s} (u, v) T dp \quad (4)$$

$$Q^L = g^{-1} L_c \int_{p_t}^{p_s} (u, v) q dp \quad (5)$$

where  $Q^S$  is total sensible heat flux (unit:  $\text{Jm}^{-1}\text{s}^{-1}$ ), and  $Q^L$  is total latent heat flux (unit:  $\text{Jm}^{-1}\text{s}^{-1}$ ). The vertical integration is from the top ( $p_t = 10 \text{ hPa}$ ) to the bottom ( $p_s = 1000 \text{ hPa}$ ) of the atmosphere,  $c_p = 1004 \text{ JK}^{-1}\text{kg}^{-1}$  is the specific heat of dry air at constant pressure,  $T$  is temperature (K),  $L_c = 2.5 \times 10^6 \text{ Jkg}^{-1}$  is the latent heat of condensation,  $u$  and  $v$  are horizontal wind velocity ( $\text{m s}^{-1}$ ),  $q$  is specific humidity<sup>19</sup>. Column-integrated moist static energy is calculated as:

$$\hat{h} = C_p \hat{T} + L_v \hat{q} + g \hat{Z} \quad (6)$$

where  $Z$  is geopotential height,  $\hat{()}$  were vertically integrated from the top and to the bottom of the atmosphere.

$$\text{meridional MSE flux} = g^{-1} \int_{p_t}^{p_s} (C_p \hat{T} + L_v \hat{q} + g \hat{Z}) \cdot v dp \quad (7)$$

For the components of MSE budget: Local variation of MSE is  $\frac{\partial \hat{h}}{\partial t}$ , lateral advection of sensible heat:  $-\vec{\nabla} C_p T \vec{u}$ , lateral advection of latent heat:  $-\vec{\nabla} L_v q \vec{u}$ , lateral advection of latent heat:  $-\vec{\nabla} L_v q \vec{u}$ , lateral advection of MSE:  $-\vec{\nabla} \hat{h} \vec{u}$ ,  $\vec{\nabla}$  is the partial derivative operator at the pressure coordinate,  $\vec{u}$  is the horizontal wind velocity (unit:  $\text{m s}^{-1}$ ).

The meridional heat energy transport (unit: PW) is calculated by discretely integrating the meridional heat flux components ( $F_v$ ), including meridional sensible heat flux, meridional latent heat flux and meridional MSE flux along the longitudinal direction of each AR basin. To account for Earth's spherical geometry, the longitudinal distances are normalized using

great circle distances. The formula is:

$$E_{transport}(\varphi) = \frac{1}{10^{15}} \sum_i [F_v(i, \varphi) \times a \cos \varphi \times \Delta \lambda] \quad (8)$$

where  $a$  is Earth radius,  $\varphi$  is latitude,  $F_v(i, \varphi)$  is the meridional flux at the  $i$ -th longitude grid point at latitude  $\varphi$  in each basin,  $\Delta \lambda$  is the  $1^\circ$  longitude interval in radians (equal to  $\frac{\pi}{180}$ ).

### Calculation of meridional temperature and moisture gradient

$$dt2m = - \frac{t2m[lat = i] - t2m[lat = i - \Delta]}{\Delta} \quad (9)$$

$$dq_{1000hpa} = - \frac{q[lat = i] - q[lat = i - \Delta]}{\Delta} \quad (10)$$

where  $dt2m$  is meridional temperature gradient,  $d1_{1000hpa}$  is meridional moisture gradient.  $\Delta$  represents temperature/moisture gradient with respect to a latitude decrement of delta  $\Delta$  degree,  $t2m$  represents air surface temperature, and  $q$  represents specific humidity at 1000 hpa,  $lat$  is latitude.

### Data availability

We thank ECMWF for providing access to ERA5 data at <https://doi.org/10.24381/cds.bd0915c6>. CMIP6 model outputs are obtained from <https://aims2.llnl.gov/search/cmip6/>. The global AR data detected with the PanLu algorithm are available on Zenodo <https://zenodo.org/records/8365114><sup>23,73</sup>.

### Code availability

This study does not use custom code or mathematical algorithm that is deemed central to the conclusions.

Received: 10 April 2025; Accepted: 9 September 2025;

Published online: 17 October 2025

### References

1. Dey, D., Campino, A. A. & Döös, K. Atmospheric water transport connectivity within and between ocean basins and land. *Hydrol. Earth Syst. Sci.* **27**, 481–493 (2023).
2. Newell, R. E., Newell, N. E., Zhu, Y. & Scott, C. Tropospheric rivers?—A pilot study. *Geophys. Res. Lett.* **19**, 2401–2404 (1992).
3. James, I. N. & Anderson, D. L. T. The seasonal mean flow and distribution of large-scale weather systems in the southern hemisphere: the effects of moisture transports. *Q. J. R. Meteorol. Soc.* **110**, 943–966 (1984).
4. de Vries, A. J. A global climatological perspective on the importance of Rossby wave breaking and intense moisture transport for extreme precipitation events. *Weather Clim. Dyn.* **2**, 129–161 (2021).
5. Mundhenk, B. D., Barnes, E. A. & Maloney, E. D. All-season climatology and variability of atmospheric river frequencies over the North Pacific. *J. Clim.* **29**, 4885–4903 (2016).
6. Gershunov, A., Shulgina, T., Ralph, F. M., Lavers, D. A. & Rutz, J. J. Assessing the climate-scale variability of atmospheric rivers affecting western North America. *Geophys. Res. Lett.* **44**, 7900–7908 (2017).
7. Kamae, Y., Mei, W., Xie, S.-P., Naoi, M. & Ueda, H. Atmospheric rivers over the Northwestern Pacific: climatology and interannual variability. *J. Clim.* **30**, 5605–5619 (2017).
8. Corringham, T. W., Ralph, F. M., Gershunov, A., Cayan, D. R. & Talbot, C. A. Atmospheric rivers drive flood damages in the western United States. *Sci. Adv.* **5**, eaax4631 (2019).
9. Ralph, F. M. et al. Flooding on California's Russian River: role of atmospheric rivers. *Geophys. Res. Lett.* **33**, L026689 (2006).
10. Lamjiri, M. A., Dettinger, M. D., Ralph, F. M. & Guan, B. Hourly storm characteristics along the U.S. West Coast: role of atmospheric rivers in extreme precipitation. *Geophys. Res. Lett.* **44**, 7020–7028 (2017).

11. Lavers, D. A. et al. Winter floods in Britain are connected to atmospheric rivers. *Geophys. Res. Lett.* <https://doi.org/10.1029/2011GL049783> (2011).
12. Zhu, Y. & Newell, R. E. A proposed algorithm for moisture fluxes from atmospheric rivers. *Mon. Weather Rev.* **126**, 725–735 (1998).
13. Ralph, F. M. et al. Dropsonde observations of total integrated water vapor transport within North Pacific atmospheric rivers. *J. Hydrometeorol.* **18**, 2577–2596 (2017).
14. Hay, J. E. & Williams, P. D. *Science of Weather, Climate and Ocean Extremes*, 195–268. <https://doi.org/10.1016/b978-0-323-85541-9.00012-2> (2023).
15. Cheng, T. F. & Lu, M. Global Lagrangian tracking of continental precipitation recycling, footprints, and cascades. *J. Clim.* **36**, 1923–1941 (2023).
16. Scholz, S. R. & Lora, J. M. Atmospheric rivers cause warm winters and extreme heat events. *Nature* **636**, 640–646 (2024).
17. Gonzales, K. R., Swain, D. L., Nardi, K. M., Barnes, E. A. & Diffenbaugh, N. S. Recent warming of landfalling atmospheric rivers along the West Coast of the United States. *J. Geophys. Res. Atmos.* **124**, 6810–6826 (2019).
18. Hsu, T.-Y. et al. Response of sea surface temperature to atmospheric rivers. *Nat. Commun.* **15**, 5018 (2024).
19. Mo, R., Lin, H. & Vitart, F. An anomalous warm-season trans-Pacific atmospheric river linked to the 2021 western North America heatwave. *Commun. Earth Environ.* **3**, 127 (2022).
20. Wille, J. D. et al. The extraordinary March 2022 East Antarctica “heat” wave. Part I: Observations and meteorological drivers. *J. Clim.* **37**, 757–778 (2024).
21. Warner, M. D., Mass, C. F. & Salathé, E. P. Jr. Changes in winter atmospheric rivers along the North American West Coast in CMIP5 climate models. *J. Hydrometeorol.* **16**, 118–128 (2015).
22. Lavers, D. A., Ralph, F. M., Waliser, D. E., Gershunov, A. & Dettinger, M. D. Climate change intensification of horizontal water vapor transport in CMIP5. *Geophys. Res. Lett.* **42**, 5617–5625 (2015).
23. Zhang, L., Zhao, Y., Cheng, T. F. & Lu, M. Future changes in global atmospheric rivers projected by CMIP6 models. *J. Geophys. Res. Atmos.* **129**, e2023JD039359 (2024).
24. Lutsko, N. J. & Cronin, T. W. Increase in precipitation efficiency with surface warming in radiative-convective equilibrium. *J. Adv. Model. Earth Syst.* **10**, 2992–3010 (2018).
25. Emanuel, K. Inferences from simple models of slow, convectively coupled processes inferences from simple models of slow, convectively coupled processes. *J. Atmos. Sci.* **76**, 195–208 (2018).
26. Deng, J., Dai, A. & Xu, H. Nonlinear climate responses to increasing CO<sub>2</sub> and anthropogenic aerosols simulated by CESM1 nonlinear climate responses to increasing CO<sub>2</sub> and anthropogenic aerosols simulated by CESM1. *J. Clim.* **33**, 281–301 (2019).
27. King, J. & Brown, C. Africa’s Living Rivers: Managing for Sustainability. *Daedalus* **150**, 240–259 (2021).
28. Zhou, Y., Kim, H. & Waliser, D. E. Atmospheric river lifecycle responses to the Madden-Julian Oscillation. *Geophys. Res. Lett.* **48**, e2020GL090983 (2021).
29. Viale, M., Valenzuela, R., Garreaud, R. D. & Ralph, F. M. Impacts of atmospheric rivers on precipitation in southern South America. *J. Hydrometeorol.* **19**, 1671–1687 (2018).
30. Pan, M. & Lu, M. East Asia atmospheric river catalog: annual cycle, transition mechanism, and precipitation. *Geophys. Res. Lett.* **47**, e2020GL089477 (2020).
31. Pan, M. & Lu, M. A novel atmospheric river identification algorithm. *Water Resour. Res.* **55**, 6069–6087 (2019).
32. Lu, M. & Hao, X. Diagnosis of the tropical moisture exports to the mid-latitudes and the role of atmospheric steering in the extreme precipitation. *Atmosphere* **8**, 256 (2017).
33. Wang, G. et al. Study on sky rivers: concept, theory, and implications. *J. Hydro-Environ. Res.* **21**, 109–117 (2018).
34. Li, Z. & Ding, Q. A global poleward shift of atmospheric rivers. *Sci. Adv.* **10**, eadq0604 (2024).
35. Lavers, D. A. & Villarini, G. The nexus between atmospheric rivers and extreme precipitation across Europe. *Geophys. Res. Lett.* **40**, 3259–3264 (2013).
36. Ralph, F. M., Cordeira, J. M., Neiman, P. J. & Hughes, M. Landfalling atmospheric rivers, the Sierra Barrier Jet and extreme daily precipitation in Northern California’s Upper Sacramento River Watershed. *J. Hydrometeorol.* **17**, 1905–1914 (2016).
37. Eiras-Barca, J. et al. European West Coast atmospheric rivers: a scale to characterize strength and impacts. *Weather Clim. Extremes* **31**, 100305 (2021).
38. Pan, M., Lu, M. & Lall, U. Diversity of cross-Pacific atmospheric river main routes. *Commun. Earth Environ.* **5**, 378 (2024).
39. Starkloff, T., Stolte, J., Hessel, R., Ritsema, C. & Jetten, V. Integrated, spatial distributed modelling of surface runoff and soil erosion during winter and spring. *Catena* **166**, 147–157 (2018).
40. Dai, L., Cheng, T. F. & Lu, M. Define East Asian monsoon annual cycle via a self-organizing map-based approach. *Geophys. Res. Lett.* **48**, e2020GL089542 (2021).
41. Kamae, Y., Mei, W. & Xie, S.-P. Climatological relationship between warm season atmospheric rivers and heavy rainfall over East Asia. *J. Meteorol. Soc. Jpn. Ser. II* **95**, 2017–2027 (2017).
42. Mahoney, K. et al. Understanding the role of atmospheric rivers in heavy precipitation in the southeast United States. *Mon. Weather Rev.* **144**, 1617–1632 (2016).
43. Shields, C. A. et al. Meridional heat transport during atmospheric rivers in high-resolution CESM climate projections. *Geophys. Res. Lett.* **46**, 14702–14712 (2019).
44. Zhang, C. et al. Quantifying the impacts of atmospheric rivers on the surface energy budget of the Arctic based on reanalysis. *EGU Sphere* **2024**, 1–37 (2024).
45. Qu, S., Su, T., Han, Z., Huang, B. & Feng, G. Dominant modes and mechanisms of atmospheric rivers in East Asia. *Atmos. Res.* **289**, 106779 (2023).
46. Simpkins, G. Atmospheric river impacts on sea ice. *Nat. Rev. Earth Environ.* **4**, 295–295 (2023).
47. Liang, K., Wang, J., Luo, H. & Yang, Q. The role of atmospheric rivers in Antarctic Sea ice variations. *Geophys. Res. Lett.* **50**, e2022GL102588 (2023).
48. Box, J. E. et al. Greenland ice sheet rainfall climatology, extremes and atmospheric river rapids. *Meteorol. Appl.* **30**, e2134 (2023).
49. Mattingly, K. S. et al. Increasing extreme melt in northeast Greenland linked to foehn winds and atmospheric rivers. *Nat. Commun.* **14**, 1743 (2023).
50. Mundhenk, B. D., Barnes, E. A., Maloney, E. D. & Nardi, K. M. Modulation of atmospheric rivers near Alaska and the U.S. West Coast by northeast Pacific height anomalies. *J. Geophys. Res. Atmos.* **121**, 12751–12765 (2016).
51. Brands, S., Gutiérrez, J. M. & San-Martín, D. Twentieth-century atmospheric river activity along the west coasts of Europe and North America: algorithm formulation, reanalysis uncertainty and links to atmospheric circulation patterns. *Clim. Dyn.* **48**, 2771–2795 (2017).
52. Song, Y., Lu, M. & Wang, B. The Indo-Pacific rim at risk: how Rossby waves contribute to extreme precipitation clustering. *Geophys. Res. Lett.* **51**, e2023GL107690 (2024).
53. Lavers, D. A. et al. Future changes in atmospheric rivers and their implications for winter flooding in Britain. *Environ. Res. Lett.* **8**, 034010 (2013).
54. Lu, M., Lall, U., Schwartz, A. & Kwon, H. Precipitation predictability associated with tropical moisture exports and circulation patterns for a major flood in France in 1995. *Water Resour. Res.* **49**, 6381–6392 (2013).
55. Trenberth, K. E. & Caron, J. M. Estimates of meridional atmosphere and ocean heat transports. *J. Clim.* **14**, 3433–3443 (2001).

56. Wang, B., Lee, M.-Y., Xie, Z., Lu, M. & Pan, M. A new Asian/North American teleconnection linking clustered extreme precipitation from Indian to Canada. *NPJ Clim. Atmos. Sci.* **5**, 90 (2022).
  57. Zhao, Y., Li, J., Tian, Y. & Li, J. Distinguish extreme precipitation mechanisms associated with atmospheric river and non-atmospheric river in the Lower Yangtze River Basin. *J. Clim.* <https://doi.org/10.1175/jcli-d-23-0400.1> (2024).
  58. Bonne, J. et al. The summer 2012 Greenland heat wave: in situ and remote sensing observations of water vapor isotopic composition during an atmospheric river event. *J. Geophys. Res. Atmos.* **120**, 2970–2989 (2015).
  59. Clark, J. P., Feldstein, S. B. & Lee, S. Moist static energy transport trends in four global reanalyses: are they downgradient? *Geophys. Res. Lett.* **49**, e2022GL098822 (2022).
  60. Zelinka, M. D. & Hartmann, D. L. Climate feedbacks and their implications for poleward energy flux changes in a warming climate. *J. Clim.* **25**, 608–624 (2012).
  61. Zhang, W. et al. Subseasonal-to-seasonal (S2S) prediction of atmospheric rivers in the Northern Winter. *NPJ Clim. Atmos. Sci.* **7**, 275 (2024).
  62. Gonzales, K. R., Swain, D. L., Barnes, E. A. & Diffenbaugh, N. S. Moisture- versus wind-dominated flavors of atmospheric rivers. *Geophys. Res. Lett.* **47**, e2020GL090042 (2020).
  63. Zhou, Y. et al. Characteristics and variability of winter Northern Pacific atmospheric river flavors. *J. Geophys. Res. Atmos.* **127**, e2022JD037105 (2022).
  64. Gao, S. & Li, X. *Cloud-resolving Modeling of Convective Processes*, 137–146. [https://doi.org/10.1007/978-1-4020-8276-4\\_9](https://doi.org/10.1007/978-1-4020-8276-4_9) (2008).
  65. Zhang, L., Zhao, Y., Cen, Y. & Lu, M. Deep learning-based precipitation simulation for tropical cyclones, mesoscale convective systems, and atmospheric rivers in East Asia. *J. Geophys. Res. Atmos.* **129**, e2024JD041914 (2024).
  66. Liang, J. & Yong, Y. Climatology of atmospheric rivers in the Asian monsoon region. *Int. J. Clim.* **41**, E801–E818 (2021).
  67. DeFlorio, M. J. et al. From California’s extreme drought to major flooding: evaluating and synthesizing experimental seasonal and subseasonal forecasts of landfalling atmospheric rivers and extreme precipitation during Winter 2022/23. *Bull. Am. Meteorol. Soc.* **105**, E84–E104 (2024).
  68. Han, J. & Singh, V. P. Impacts of Rossby wave packets and atmospheric rivers on meteorological drought in the continental United States. *Water Resour. Res.* **57**, e2021WR029966 (2021).
  69. Young, Z. M., Martens, H. R., Hoylman, Z. H. & Gardner, W. P. Drought characterization with GPS: insights into groundwater and surface-reservoir storage in California. *Water Resour. Res.* **60**, e2024WR037404 (2024).
  70. Hersbach, H. et al. ERA5 hourly data on pressure levels from 1940 to present. Copernicus Climate Change Service (C3S) Climate Data Store (CDS). <https://doi.org/10.24381/cds.bd0915c6> (2023).
  71. Eyering, V. et al. Overview of the Coupled Model Intercomparison Project Phase 6 (CMIP6) experimental design and organization. *Geosci. Model. Dev.* **9**, 1937–1958 (2016).
  72. Wu, X., Hao, Z., Zhang, Y., Zhang, X. & Hao, F. Anthropogenic influence on compound dry and hot events in China based on Coupled Model Intercomparison Project Phase 6 models. *Int. J. Clim.* **42**, 4379–4390 (2022).
  73. Zhang, L. Atmospheric River database. Zenodo <https://doi.org/10.5281/zenodo.8365114> (2023).
- Kong Research Grants Council, NSFC/RGC Collaborative Research Scheme (project no. CRS\_PolyU503/23). The authors are grateful for the support from Otto Poon Centre for Climate Resilience and Sustainability, HKUST. This study is part of the UNESCO International Decade of Sciences for Sustainable Development (IDSSD, 2024–2033) and contributes to the Seamless Prediction and Services for Sustainable Natural and Built Environment (SEPRESS) Program (2025–2032), an initiative endorsed under this UNESCO IDSSD framework. We gratefully acknowledge the European Centre for Medium-Range Weather Forecasts (ECMWF) for providing ERA5, the Working Group on Coupled Modelling under the World Climate Research Programme (WCRP), and the climate modeling groups for providing the CMIP6 model outputs.

### Author contributions

M. Lu and Y. Song contributed to the conceptualization, methodology, investigation, data analysis, visualization, original draft preparation, and manuscript revisions. W. Huang contributed to the conceptualization and data analysis. L. Zhang contributed to data acquisition and methodology. All authors participated in the discussion of the results and manuscript writing.

### Competing interests

The authors declare no competing interests.

### Additional information

**Supplementary information** The online version contains supplementary material available at <https://doi.org/10.1038/s43247-025-02780-6>.

**Correspondence** and requests for materials should be addressed to Mengqian Lu.

**Peer review information** *Communications Earth and Environment* thanks the anonymous reviewers for their contribution to the peer review of this work. Primary handling editors: Chao He, Aliénor Lavergne, and Alice Drinkwater. A peer review file is available.

**Reprints and permissions information** is available at <http://www.nature.com/reprints>

**Publisher’s Note** Springer Nature remains neutral with regard to jurisdictional claims in published maps and institutional affiliations.

**Open Access** This article is licensed under a Creative Commons Attribution-NonCommercial-NoDerivatives 4.0 International License, which permits any non-commercial use, sharing, distribution and reproduction in any medium or format, as long as you give appropriate credit to the original author(s) and the source, provide a link to the Creative Commons licence, and indicate if you modified the licensed material. You do not have permission under this licence to share adapted material derived from this article or parts of it. The images or other third party material in this article are included in the article’s Creative Commons licence, unless indicated otherwise in a credit line to the material. If material is not included in the article’s Creative Commons licence and your intended use is not permitted by statutory regulation or exceeds the permitted use, you will need to obtain permission directly from the copyright holder. To view a copy of this licence, visit <http://creativecommons.org/licenses/by-nc-nd/4.0/>.

© The Author(s) 2025

### Acknowledgements

This research is supported by the Collaborative Research Funds (C6032-21G, C5004-23G, and C5002-22Y), General Research Fund (16300424) of the Hong